Petroleum Science 19 (2022) 2399–2412

Contents lists available at ScienceDirect

Petroleum Science

journal homepage: www.keaipublishing.com/en/journals/petroleum-science

Original Paper

Numerical study on the strain capacity of girth-welded X80 grade pipes

Xu Wang [a, b], Jian Shuai [a, *], Sheng-Zhu Zhang [c], Wei Ren [a], Xue-Ming Zhu [a]

[a] College of Safety and Ocean Engineering, China University of Petroleum, Beijing, 102249, China
[b] Department of Structural Engineering, Norwegian University of Science and Technology (NTNU), Trondheim, 7491, Norway
[c] China Academy of Safety Science and Technology, Beijing, 100012, China

ARTICLE INFO

Article history:
Received 5 August 2021
Accepted 22 March 2022
Available online 14 April 2022

Edited by Xiu-Qiu Peng

Keywords:
Strain capacity
Girth-welded
X80 grade pipes
Mismatch and softening

ABSTRACT

Strain capacity is an important performance indicator for designing and evaluating high-grade steel pipelines. Due to the inhomogeneity of material properties in welded structures, girth welds are one of the main factors that restrict the strain capacity of pipelines. In this paper, girth-welded pipes with cracks in the inner surface of the weld have been studied, and the ductile crack initiation and propagation behavior have been simulated using the Gurson model. The corresponding nominal strain at the onset of crack initiation was defined as the characteristic value of strain capacity. The influencing factors on the strain concentration area, strain concentration factor, and strain capacity of girth-welded pipes were quantitatively analyzed. A semiempirical calculation formula for the strain capacity of typical girth-welded X80 grade pipes has been proposed as a function of the crack size, mismatch coefficient of the weld, and softening degree of the heat affected zone (HAZ). This study can facilitate the defect assessment of girth-welded pipes.

1. Introduction

With the wide application of high-strength steels in the oil and gas transport industry, the strain-based assessment method for pipelines has received increasing attention aiming to make full use of its plastic strain capacity (Panico et al., 2017; Revie, 2015). However, defects in the welding process of pipeline girth welds are almost inevitable, even if extremely stringent quality control procedures are enforced. With increasing service time, these defects may propagate to a critical size that could endanger the safety of pipelines. Coupled with factors such as discontinuous microstructures and inconsistent materials in welded structures, girth welds have become one of the main factors limiting the strain capacity of pipelines (Maddox, 2014).

The strain capacity of girth-welded pipes is affected by factors such as the weld geometry, defect size, level of weld metal mismatch, degree of softening and internal pressure (Bastola et al., 2016). Experiments, numerical simulations, or a combination of both have been used for the study of strain capacity in the literature. Kyriakides et al. (Kyriakides and Corona, 2007), provided a global strain calculation method (no defects considered) when using the reel-lay method to lay subsea pipelines. Østby et al. (Ostby and Hellesvik, 2008), tested the strain capacity in SENT (single edge notched tension) specimens with defects both in the base material and in weldments and noted that the overmatch led to an increase in strain capacity. Wang et al. (2011), developed a conservative tensile strain capacity equation with fewer parameters for welded pipelines. Igi et al. (2011), examined the effect of internal pressure on the tensile strain capacity of pipelines through the pressurized full-pipe tension test and curved wide plate (CWP) test and found that the critical tensile strain drops sharply with high internal pressure. Hertele et al. (2016), validated an upper bound equation of tensile strain capacity using 64 curved wide plate test results and developed a strain capacity prediction method for mismatched welding. Abdulhameed and Agbo et al. (Abdulhameed et al., 2016; Agbo et al., 2019), investigated the effect of internal pressure and flaw size on the tensile strain capacity through full-scale tests of X52 and X42 pipes using biaxial strain gauges and a digital image correlation (DIC) system. Hohler et al. (2016), took a series of full-scale 4-point bending tests of X70 welded pipes subject to internal pressure and concluded that the

* Corresponding author.
E-mail address: shuaij@cup.edu.cn (J. Shuai).

https://doi.org/10.1016/j.petsci.2022.04.009

Nomenclature

a	Crack depth
c	Half crack length
D	The outer diameter of pipe
E	Elastic modulus
f	Void volume fraction
f_0	Initial void volume fraction
f_c	Critical void volume fraction
f_F	Failure void volume fraction
f^*	Effective void volume fraction
f_u	Ultimate void volume fraction
M	Welded mismatch coefficient
n	Strain hardening exponent
q_1, q_2, q_3	Constitutive parameters of GTN model
S	Degree of softening in HAZ
t	Wall thickness of pipe
Y/T	Yield to tensile strength ratio
α	Strain hardening coefficient
$\overline{\sigma}$	Flow stress of the matrix material
σ_e	Engineering stress
σ_{eq}	von Mises equivalent stress
σ_m	Hydrostatic stress
σ_T	Tensile strength
σ_Y	Yield strength
ε_Y^e	Elastic strain at the yield strength
σ_{YB}	Yield strength in base metal
σ_{YW}	Yield strength in weld metal
ε_c	Strain capacity
υ	Poisson's ratio
φ	Yield function

girth weld has a significant influence on the axial strains and that the strip end weld of the HSAW pipe increased the bending stiffness.

Full-scale experiments, which are an important means to study the strain capacity of girth-welded pipes, are limited by factors such as equipment, technology, and cost. Therefore, it is unrealistic to conduct a large number of tests accounting for all these factors, and the method of combining numerical simulations and experiments has become a good auxiliary research method. Hertelé et al. (Hertelé et al., 2013, 2014; Verstraete et al., 2014), confirmed that the CWP specimens seem to be a good representative of the constraints in pipe specimens in the case of mismatched welding. They performed a large series of finite element analysis (FEA) simulations and tests of CWPs to quantify the effect of pipe steel heterogeneity on strain capacity and proposed a new strain capacity equation. Van Minnebruggen et al. (Van Minnebruggen et al., 2015), investigated the effect of the pipe forming angle, weld strength overmatch and material strength anisotropy on tensile strain capacity and emphasized that ignoring anisotropy in FEA may overestimate the strain capacity. Bastola et al. (2017), carried out a literature review, small-scale testing, full-scale pipe bending and reeling tests, and detailed FEA to investigate the strain capacity of girth-welded X80 pipes. The full-scale reeling tests showed that the welded X80 pipes could withstand 2.5% strain in the range of flaw sizes considered. Zhao et al. (2019), proposed an optimized reference strain approach based on a large number of FEAs, considering assessment conditions such as ultralow mismatch welds (below 0.8) and clads. Det Norske Veritas (DNV) (Submarine pipeline systems) advised using damage models to simulate crack growth for the design of submarine pipelines. Testa et al. (2017), proposed a continuum damage mechanics (CDM) model to predict the strain capacity of X65 steel, which performed well in predicting ductile crack growth of single-edge notched bending (SENB) and SENT fracture specimens. The Gurson-Tvegaar-Needleman (GTN) model has been the method most often used to simulate the ductile fracture process consisting of nucleation, growth, and coalescence of microvoids (Zhu, 2015). Qiang et al. (Qiang and Wang, 2019), calibrated the GTN model parameters in the inhomogeneity of the welded joint using the experimental results of SENT and SENB specimens. The calibrated GTN model could predict the crack propagation resistance curves of different weld positions under different constraints. Zhang et al. (Kibey et al., 2008; Xu et al., 2009; Zhang et al., 2000), developed a complete Gurson model (CGM) based on the modified Gurson model and the plastic limit load model by Thomason. The most attractive feature of CGMs is that ductile failure of the material is exclusively linked to the microvoid nucleation parameter. CGM was applied to study the ductile crack growth behavior of SENB and SENT specimens.

In this study, an FEA model of girth-welded pipes with cracks in the inner surface of the weld was established to study the effect of crack initiation and propagation on the strain capacity. Based on the simulation results, a semiempirical formula for describing the strain capacity is proposed, and the various influencing factors are also discussed. A detailed description of the modeling procedure used, such as the materials, GTN model, and FEA, is introduced in Section 2. The characterization method and semiempirical calculation formula of the strain capacity are proposed in Section 3. The effects of defect size, welded mismatch, softening of the heat-affected zone (HAZ), and internal pressure on the strain capacity of girth-welded pipes are discussed in Section 4. The results of this study will supply a reference for and facilitate defect assessment in girth welds of X80 grade pipes.

2. Modeling procedures

This section provides a detailed description of the models used in this paper. The stress–strain behavior of the pipeline steels is represented by the Ramberg–Osgood (R-O) model, and the GTN model is used to simulate the damage evolution process of the material. The FEA model of the girth-welded pipe was established using ABAQUS version 6.14.

2.1. Materials

The R-O model, Eq. (1), is widely used for the description of the constitutive behavior of pipeline steels in the literature and engineering design guidelines and is also adopted to characterize the stress–strain curves of the materials considered in this study. The R-O model can be expressed as:

$$\frac{\varepsilon}{\varepsilon_Y^e}=\frac{\sigma}{\sigma_Y}+\alpha\left(\frac{\sigma}{\varepsilon_Y}\right)^n \tag{1}$$

where σ_Y is the yield strength, ε_Y^e is the elastic strain at the yield strength, α is the strain hardening coefficient, and n is the strain hardening exponent. α can be calculated by the following formula:

$$\alpha=\varepsilon_Y\cdot E/\sigma_Y-1 \tag{2}$$

where, E is Young's modulus, ε_Y is the yield strain, and $\varepsilon_Y = 0.005$.

Under the assumption that the volume is incompressible (Wang et al., 2020), Eq. (1) can be transformed into:

$$\frac{\sigma_T}{E}+\left(0.005\cdot\frac{\sigma_Y}{E}\right)\cdot n\cdot\left(\frac{\sigma_T}{\sigma_Y}\right)^n=1 \tag{3}$$

Due to the inhomogeneity of material properties in welded structures, girth welds have become one of the main factors that restrict the strain capacity of pipelines. This paper considers three types of welding conditions: undermatch, overmatch, and even match. The welding mismatch coefficient M is defined as the ratio between the yield strength in the weld metal and base metal as $M=\sigma_{YW}/\sigma_{YB}$. The softening of HAZs in high-grade pipeline steel girth welds is not uncommon and has been considered (Hertelé et al., 2014). Similarly, the degree of softening S is defined as the ratio of the yield strength in the HAZ and base metal, $S=\sigma_{YH}/\sigma_{YB}$, which means that the smaller the S value is, the higher the degree of softening.

According to API Specification 5 L: Line Pipe, the yield strength and tensile strength for the base metal of X80 pipes are selected to be 555 MPa and 625 MPa, respectively. The Young's modulus E and Poisson's ratio υ of all materials are set to 210 GPa and 0.3, respectively. The strain hardening coefficient α and strain hardening exponent n are calculated referring to Eqs. (2) and (3) (Wang et al., 2020). In the following material parameter sensitivity analysis, 7 cases for varying M values (0.85 $\sim$ 1.15) and 3 cases for varying S values (0.85 $\sim$ 0.95) were considered. Fig. 1 presents the stress-strain curves used for the subsequent numerical simulations in this paper.

2.2. GTN model and verification

The GTN model is the most widely used damage model to simulate the ductile tearing process of pipeline steel materials (Pineau, 2006). The prototype of the GTN model was first proposed by Gurson and then further refined by Tvergaard and Needleman (Gurson, 1977; Tvergaard, 1982; Tvergaard and Needleman, 1984). The GTN model can describe the process of void nucleation, evolution, and aggregation during the ductile fracture of materials. The expression of the GTN model is:

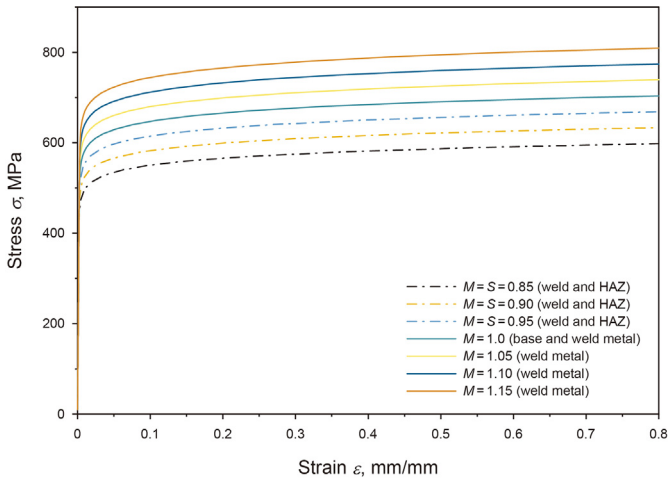

Fig. 1. The stress–strain curves used for numerical simulation.

$$\begin{cases}\varphi=\left(\dfrac{\sigma_{eq}}{\overline{\sigma}}\right)^2+2q_1f^*\cosh\left(\dfrac{3q_2\sigma_m}{2\overline{\sigma}}\right)-1-q_3(f^*)^2=0\\ f^*=\begin{cases}f & \text{for } f\le f_c\\ f_c+\dfrac{f_u^*-f_c}{f_F-f_c}(f-f_c) & \text{for} f_c<f<f_F\\ f_F & \text{for} f\ge f_F\end{cases}\end{cases} \tag{4}$$

where φ is the yield function; σ_{eq} is the von Mises equivalent stress; σ_m is the hydrostatic stress; $\overline{\sigma}$ is the flow stress of the matrix material; f^* is the effective void volume fraction, which is recommended by Tvergaard and Needleman to replace f (the void volume fraction) in the Gurson model (Tvergaardand Needleman, 1984); f_u^* is the ultimate void volume fraction; f_0 is the initial void volume fraction; f_c is the critical void volume fraction; f_F is the void volume fraction at final failure; and q_1, q_2, and q_3 are the factors introduced by Tvergaard to improve the prediction accuracy of the model. The cluster nucleation mode is one of the nucleation mechanism methods in which usability and accuracy have been verified in describing the properties of the material in pipe steel (Di et al., 2015; Sandvik et al., 2008). The value of f_F is not directly a material property but a value of plasticity development following void nucleation related to the f_0 value, and the expression was proposed by Zhang et al., $f_F=0.15+2\cdot f_0$ (Zhang, 1998; Zhang et al., 2000). q_1, q_2, and q_3 are recommended by Tvergaard, and 1, 1.5, and 2.25 are used, respectively (Tvergaardand Needleman, 1984).

To obtain the damage parameters of the GTN model suitable for simulating the X80 pipe steel material, a notched specimen was designed for the uniaxial tensile test. The geometry of the notched specimen is shown in Fig. 2(a), and the initial minimum cross-sectional radius of this specimen is $a_0=4$ mm. Fig. 3 shows the tensile test of the notched specimen. The test equipment was an MTS 810-250 kN loaded at a constant speed of 0.3 mm/min. The whole test was carried out at room temperature, and the tensile load F was recorded once per second. An industrial digital camera was used to record the deformation of the notched specimen during the tensile test (once per second). After the tensile test, the average true strain ε was calculated from the minimum cross-sectional area reduction (Tu et al., 2017, 2019):

$$\varepsilon=2\cdot\ln(a_0/a_i) \tag{5}$$

where a_i is the instantaneous minimum cross-section radius, which can be measured by digital image computing technology. The engineering stress σ_e can be calculated by dividing the tensile load F by the initial minimum cross-sectional area.

$$\sigma_e=F\Big/\left(\pi\cdot a_0^2\right) \tag{6}$$

A 1/4 axisymmetric finite element analysis (FEA) model was established to simulate the entire tensile test of the notched specimen, as shown in Fig. 2(b). The element type of the FEA model was selected as CAX4R, solved by ABAQUS/Explicit, and the NLGEOM option was also activated. The density of the steel material was set to 7800 kg/m^3 (Han et al., 2014). The stress–strain curve of the material is based on Eq. (1). The element size at the minimum cross-section was set as 0.125 mm (Liu and Wang, 2006). The average true strain ε and engineering stress σ_e can be calculated by Eqs. (5) and (6).

The tensile test and FEA simulation results of the notched

specimen are shown in Fig. 4. The scattered points in the figure are the test results, and the curve is the FEA simulation result. Many simulations have been performed to obtain the best fitting curve. The input parameters for this simulation are $E = 210$ GPa, $n = 18$, $\upsilon = 0.3$, and $\sigma_Y = 565$ MPa, and the other GTN-related damage parameters are shown in Table 1. The stress contours corresponding to the failure of the notched specimen are shown in Fig. 4. The simulated failure position is located at the center of the minimum cross-section of the notched specimen, consistent with the experimental observation results.

2.3. FEA model

The geometries of pipe and girth welds depend on the actual parameters of pipes without loss of generality. The weld metal in Fig. 5 is distinguished by dark color. The pipe diameter and wall thickness were set to 1219 mm and 18.4 mm, respectively. As shown in Fig. 5(b), the angle of the Single-V groove welded joint was set to 30°, and then the root gap, root face, root reinforcement, and face reinforcement were set as 4.0 mm, 3.0 mm, 0.5 mm, and 1.0 mm, respectively. The width of the HAZ was set as 3 mm, and the defect was a crack of constant depth; refer to Fig. 5(b) and (c) for details. In subsequent calculations, a total of 9 types of defect sizes were considered, including three depths ($a/t = 0.3$, 0.4, 0.5) and three lengths ($2c = 50$ mm, 100 mm, 150 mm).

To simulate the ductile fracture process in the girth-weld pipe shown in Figs. 5 and 3D elastic–plastic FEA was performed using the ABAQUS/Explicit solver, and the NLGEOM option in ABAQUS was also activated for large-strain nonlinear geometry analysis. Material mechanical properties and GTN-related damage parameters were implemented according to Chapters 2.1 and 2.2, respectively. A quarter of the pipe with an inner surface crack in the middle of the weld was modeled with the C3D8R element, considering the symmetry of the pipeline, as shown in Fig. 6. The element size in the crack growth zone (including the crack tip and crack front shown in Fig. 6(c)) was set as 0.125 mm, which is generally recommended to range from 0.1 to 0.3 mm for steel (Liu and Wang, 2006). The structured transitional mesh was also used from the high degree of mesh refinement at the crack region to the larger elements in the rest of the model to speed up the calculation. The axial length of the 1/4 model is 2500 mm, and a uniform displacement load is applied at the remote section away from the crack. The number of elements varies from 125,000 to 132,000 depending on the crack size of the models. A half-circle (shown in Fig. 6(d)) was used to describe the shape of the crack tip, the radius of which was equal to the element size of the crack front. This kind of structure has been proven to have a good effect in simulating the blunting process of crack tips, and the simulation results are in good agreement with the test results (Cravero et al., 2008; Østby et al., 2008).

3. Strain capacity of girth-welded pipes

3.1. Failure criterion

In this study, the crack tip opening displacement (CTOD) was selected as the parameter describing both the driving force and resistance. Fig. 7(a) shows the calculation method of CTOD in the postprocessing of FEA, which uses the mirror function of the software to complete the crack profile. The crack growth resistance curve, also called the R-curve, was defined as the plot of the resistance to fracture versus crack extension. Fig. 7(b) shows the curves between the remote average strain at different positions in the axial direction away from the crack as the displacement load increases. Since the local strain is affected by factors such as weld mismatch, softening of the HAZ, and defects, the nominal strain of the remote pipe was selected as the representative value of the strain instead of the local strain. When the distance from the crack exceeds 500 mm, the axial strain of the pipe is a constant that does not change with the distance. The average nominal strain at the far end of the pipe at a distance of 1000 mm from the crack was selected as the strain characterization value in the following sections.

R-curves under three different crack cases are shown in Fig. 8. When $\Delta a = 0.125$ mm, the strain state of the crack tip when crack initiation occurs is also shown in Fig. 8. The corresponding CTOD is

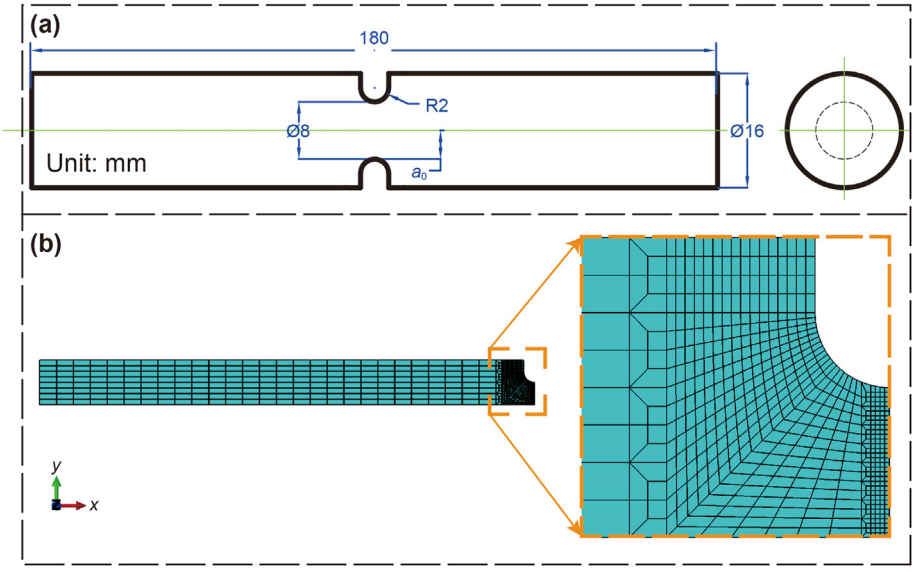

Fig. 2. The geometry and FEA model of the notched specimen.

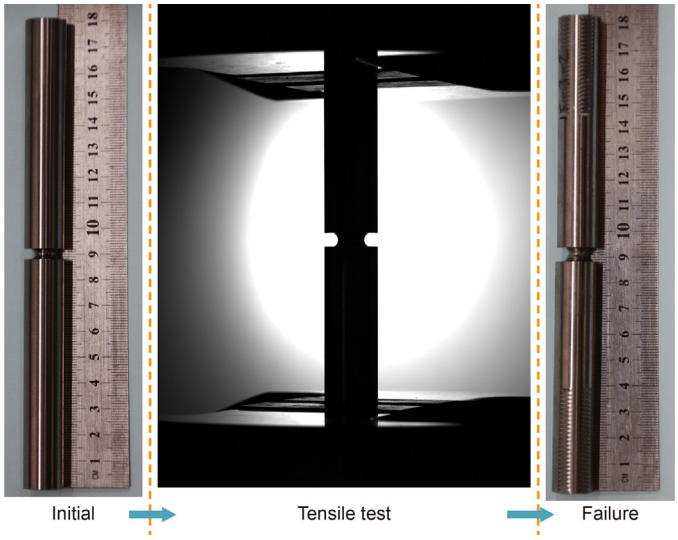

Fig. 3. The uniaxial tensile test of notched specimen.

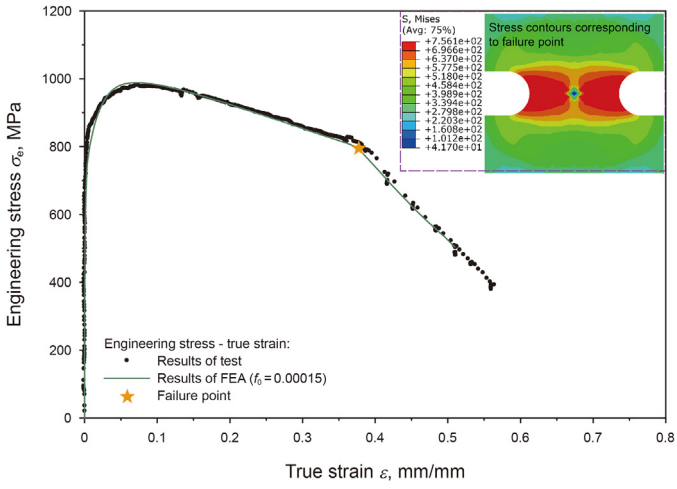

Fig. 4. Results of the tensile test and FEA simulation of the notched specimen.

selected as the critical CTOD to ensure conservativeness. The remote average nominal at the far end of the pipe corresponding to the critical CTOD is defined as the strain capacity of the girth-welded pipe in this study.

3.2. Strain capacity

As mentioned above, the corresponding nominal strain away from the crack at the onset of crack initiation was defined as the characteristic value of the strain capacity. A total of 189 sets of FEA data were used to fit the semiempirical calculation formula of the strain capacity of the girth-welded pipe. The mismatch coefficient (M), softening coefficient (S) and defect size (c, a) are considered separately in this formula. The fitting formula is as follows:

Table 1
Parameters for GTN model.

f_0	f_c	f_F	q_1	q_2	q_3
0.00015	0.013	0.1503	1.5	1	2.25

$$\varepsilon_c = \beta_0 + \beta_1 \cdot \exp\left(-\frac{1}{\beta_2}\frac{4c}{D} - \frac{1}{\beta_3}\frac{a}{t}\right) + \beta_4 \cdot \left(\frac{4c}{D}\right)^2 + \beta_5 \cdot \left(\frac{a}{t}\right)^2 + \beta_6 \cdot \left(\frac{4c}{D}\right) \cdot \left(\frac{a}{t}\right) \tag{7}$$

where ε_c is the strain capacity; β_i is the fitting parameter, $i = 0,1,2 \ldots 6$, refer to Table 2 for the value of β_i; c is the half length of crack, mm; a is the depth of crack, mm; D is the outer diameter of the pipe, D = 1219 mm; and t is the wall thickness of the pipe, t = 18.4 mm. Simultaneously, the calculation results of the fitting formula were compared with the finite element results for error analysis. The average error does not exceed 5%, and the maximum error is 8.21%, indicating that the fitting formula has high accuracy. The applicable range of Eq. (3) is M = 0.85–1.15, S = 0.85–0.95, a = 0.3t - 0.5t, 2c = 50 mm–150 mm, and the average error is within 5%, which can meet the requirements of strain-based assessment in engineering. It should be clarified that the above proposed strain capacity estimation formula (Eq. (3)) is only applicable to X80 girth welded pipes, and the absolute value of strain capacity is also extremely dependent on the damage parameters of the material. For the material of X80 girth welded pipe investigated in this paper, the damage parameters are shown in Table 1, where the f_0 and f_c are the key parameters.

4. Results and discussion

The effects of the defect size, mismatched weld, softening of the HAZ, and internal pressure on the strain concentration and strain capacity of girth-welded pipes are discussed in this section.

4.1. Effect factors of strain concentration

4.1.1. Defect size

Fig. 9(a) shows the strain contours in the local area of a girth-weld pipe when the remote strain is 0.5% at different crack sizes. We can observe whether there is plastic deformation and strain concentration in the material in this local area from Fig. 9. The gray area is the area where the strain exceeds 0.5%, which means that the material in these areas has been plastically deformed, and there is a certain degree of strain concentration. When the defect size is fixed, the size of the gray area gradually increases with increasing remote strain (0.1%–0.5%), and the growth rate decreases. When the remote strain increases from 0.1% to 0.3%, the gray area changes significantly. When the remote strain increases from 0.3% to 0.5%, the gray area remains more or less constant.

Fig. 9(b) shows the curves of the strain concentration factor at the crack tip. The strain concentration factor is defined as the ratio of the logarithmic strain of the crack tip to the remote logarithmic strain. The abscissa of the end of the curve is the corresponding remote strain when the crack starts to grow, and the value is equal to the strain capacity value defined in the previous chapter. As the crack size increases (both depth and length), the girth-welded pipe strain capacity gradually decreases, and the peak value of the strain concentration factor gradually increases. The crack will start to grow when the strain concentration factor is in the descending stage of the curve for a crack length of 50 mm. However, for the 150 mm crack, it is in a rising channel because, under different defect conditions, the degree of plastic deformation of the material at the crack tip and remote is different.

Fig. 10 and Fig. 11 show the strain contours and strain concentration factors under even-matching (M = 1.0) and overmatching (M = 1.1) welds, respectively. From these figures, we can observe

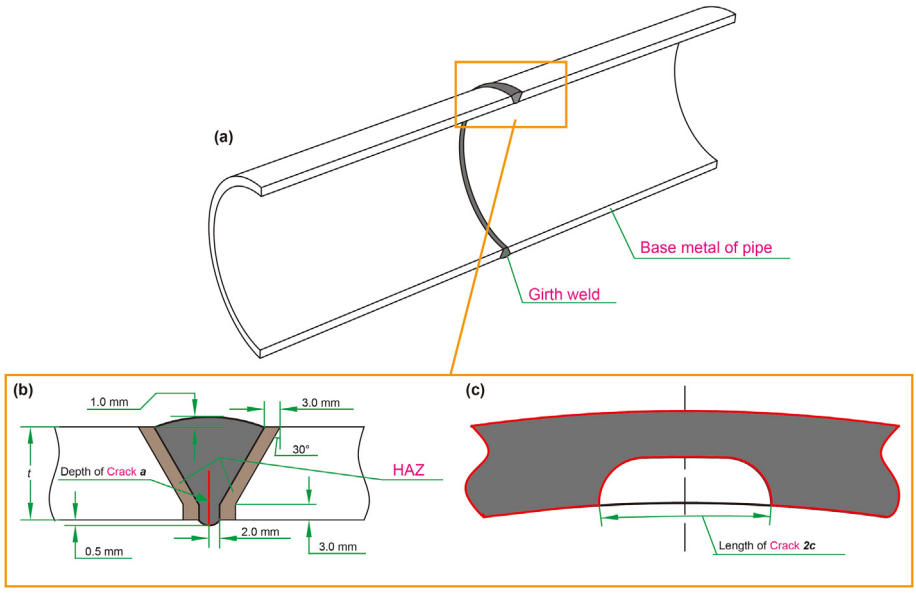

Fig. 5. Geometries of pipe and girth weld: pipe with girth weld (a), the single-V groove weld joint with crack (b) and the crack of constant depth (c).

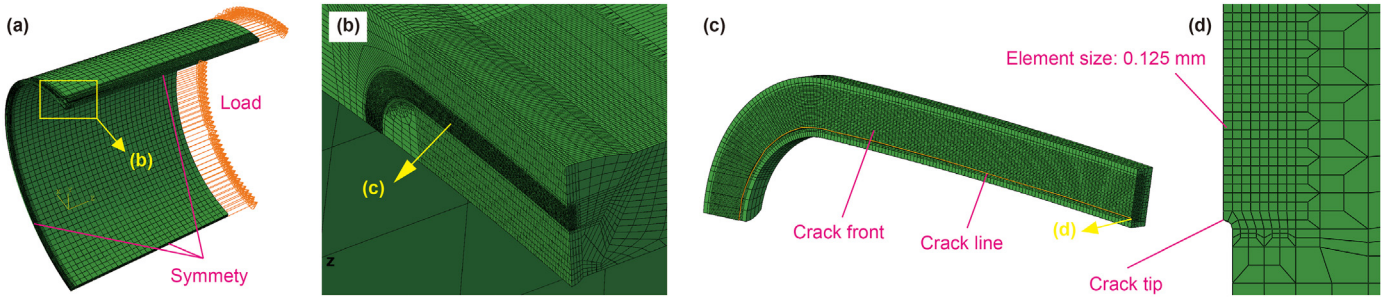

Fig. 6. The finite element model for the girth-welded pipe: a quarter of the pipe (a), the inner surface crack in the middle of the weld (b), the crack front (c), and the crack tip (d).

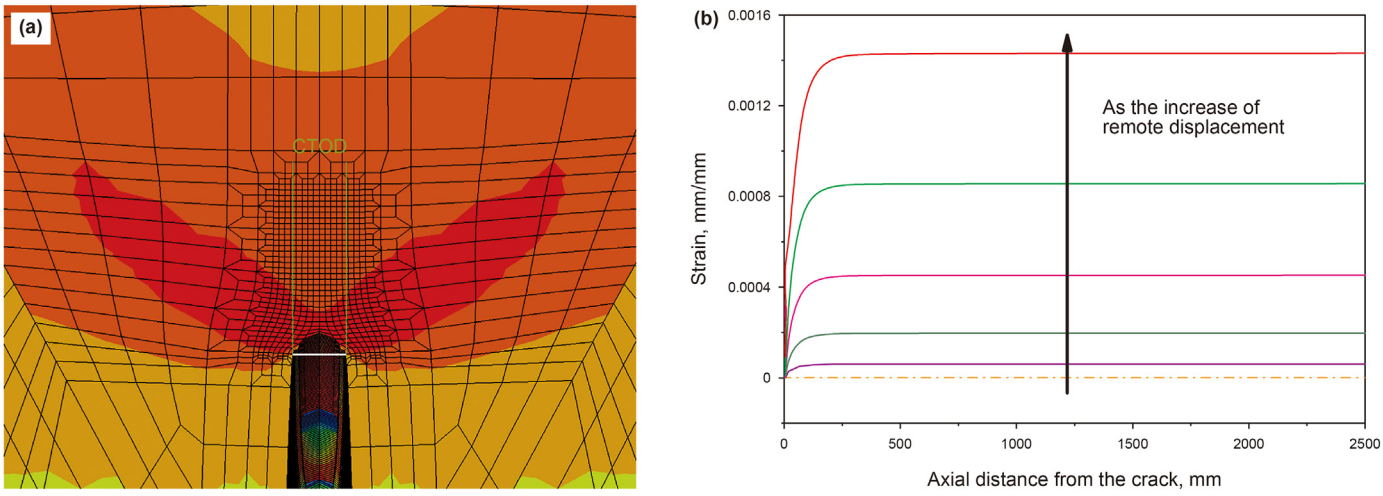

Fig. 7. The calculation method of CTOD (a) and strain (b) in the postprocessing of FEA.

results similar to the figures drawn from undermatching ($M = 0.9$) in Fig. 9. The difference is that the size of the gray areas is different under the same defect size and remote strain conditions, especially obvious when the defect size is small. Take the crack ($a/t = 0.3$, $2c = 50$ mm) and the remote strain (0.3%) as an example. As M increases, the size of the gray areas gradually decreases. When $M = 1.1$, only when the defect size is $a/t = 0.3$ and $2c = 50$ mm will the crack start to grow when the strain concentration factor is in

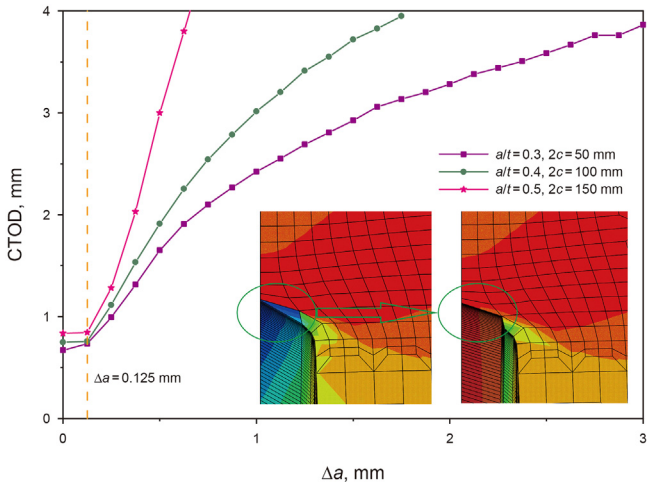

Fig. 8. The R-curves and failure criterion.

the rising channel indicating that with an increase in M, the base metal of the girth-welded pipe has greater plastic deformation under the abovementioned failure criterion. It can be observed that in Figs. 9(b), 10(b) and 11(b), the strain concentration are very large when the remote strain are about equal to 0.25% then decreases rapidly. The primary reason for this phenomenon is the difference in the degree of plastic deformation caused by the localization of the weld and the remote part of the pipe. The level of plastic deformation in the weld is associated with the material damage parameters, defect size, weld matching coefficient, heat affected zone softening, internal pressure, and other factors.

4.1.2. Mismatch of girth-welded pipes

Fig. 12 more intuitively shows the effect of the weld mismatch coefficient (M) on the strain contours and strain concentration factors. Fig. 12(a) is the result of defect ($a/t = 0.3$, $2c = 50$ mm). Fig. 12(b) shows the comparison result of defects ($a/t = 0.3$, $2c = 50$ mm and $a/t = 0.5$, $2c = 150$ mm). Fig. 12(a) further verifies the above conclusion. That is, as M increases, the size of the gray area (strain concentration area) gradually decreases. When remote strain increases from 0.3% to 0.5%, the magnitude of change in the gray area will also be affected by M. When M is large, the trend of change is more obvious. Fig. 12(b) shows that the strain concentration factor corresponding to the case with the larger defect size is significantly larger than the strain concentration factor of the small defect size because when the defect size is larger and the same remote strain is used, the plastic deformation in the base metal of the girth-weld pipes is smaller. Therefore, we can conclude that an overmatched weld in girth-welded pipes can increase the local strength of the weld metal and significantly reduce the strain concentration. However, the variability between the strain concentration curves with different matching factors is smaller (the curves are closer) at larger defect sizes.

4.1.3. Softening of HAZ

In the above discussion, the softening degree of the HAZ (S) was fixed at 0.9. Below, we will discuss the impact of S. Fig. 13 shows the effect of S at different M values on the corresponding strain contours and strain concentration factors. The data in Fig. 13(a) are the result of defects ($a/t = 0.3$, $2c = 50$ mm). When the remote strain is 0.2%, the strain concentration area is still around the crack tip. When the remote strain increases to 0.25%, the strain concentration area spreads to the HAZ and extends to the outer wall along the boundary of the HAZ. There is no large difference in the size of the gray area under different S. Therefore, the softening of the HAZ is also one of the main reasons that caused the strain concentration, but the degree of softening (S) has little effect on the strain concentration, which can also be verified in Fig. 13(b). The difference in the curves of the strain concentration factors is relatively close for different S values with the same M. The effect of S in the undermatched weld is more obvious than matching the overmatched weld, mainly because the material selected in this paper has a small range degree of softening. However, the range degree of softening is also limited to the location of the defect and the size of the HAZ.

4.1.4. Internal pressure

The above are all discussions considering only the axial displacement load. Fig. 14 results from considering the influence of internal pressure on the strain contours and strain concentration factors. Based on the previous conclusions, this section discusses only the defect results ($a/t = 0.3$, $2c = 50$ mm) when S is 0.9. For the strain concentration area, when the internal pressure increases from 4 MPa to 8 MPa, the size of the strain concentration area

Table 2
The fitting parameters for strain capacity.

M	S	β_0	β_1	β_2	β_3	β_4	β_5	β_6	Maximum error	Average error
1	0.95	0.31290	−0.23846	−0.65517	−1.29732	0.98074	0.24157	0.65345	6.34%	2.10%
1	0.9	33.87140	−33.80632	−115.75795	−257.36548	0.48351	0.09482	0.18208	4.87%	1.47%
1	0.85	0.51973	−0.45091	−1.49028	−3.06471	0.60310	0.13457	0.31546	5.58%	2.11%
1.05	0.95	0.39300	−0.29291	−0.68404	−1.03570	1.08501	0.42524	0.95633	6.22%	3.77%
1.05	0.9	40.10911	−40.03059	−128.09406	−246.42332	0.49885	0.11582	0.19044	6.33%	2.07%
1.05	0.85	1.71220	−1.63590	−5.16753	−12.04396	0.52619	0.08217	0.21437	7.50%	2.43%
1.1	0.95	0.48183	−0.35949	−0.76909	−1.07423	1.10815	0.48244	0.98912	5.10%	1.48%
1.1	0.9	0.46342	−0.36120	−0.97999	−1.54949	0.80337	0.26161	0.54039	4.70%	1.65%
1.1	0.85	1.53794	−1.45567	−5.48141	−10.60797	0.43972	0.07138	0.13135	6.34%	2.82%
1.15	0.95	0.40213	−0.27820	−0.81521	−0.79857	0.56190	0.56016	1.05771	8.21%	4.56%
1.15	0.9	0.82385	−0.59211	−0.62803	−0.74645	2.33058	1.46750	3.11672	7.28%	2.59%
1.15	0.85	0.81051	−0.57935	−0.63652	−0.77793	2.34566	1.34266	2.74446	5.56%	2.67%
0.95	0.95	0.81051	−0.57935	−0.63652	−0.77793	2.34566	1.34266	2.74446	5.56%	2.67%
0.95	0.9	0.24186	−0.18226	−0.50759	−1.41555	1.09770	0.15019	0.63547	7.78%	3.43%
0.95	0.85	0.29557	−0.24571	−0.86123	−3.01604	0.66878	0.05781	0.30945	7.24%	3.30%
0.9	0.95	0.15945	−0.11647	−0.35285	−1.37012	1.32690	0.09637	0.61465	3.48%	1.00%
0.9	0.9	0.17316	−0.12659	−0.35343	−1.31133	1.43343	0.11270	0.70137	3.05%	1.06%
0.9	0.85	0.15788	−0.11473	−0.29648	−1.79505	1.78143	0.04779	0.58881	7.27%	2.18%
0.85	0.95	0.09906	−0.07171	−0.32338	−1.34675	0.97292	0.06402	0.41450	5.31%	2.01%
0.85	0.9	0.10435	−0.07543	−0.28571	−1.51408	1.26978	0.04799	0.46802	2.02%	0.84%
0.85	0.85	0.10613	−0.07670	−0.26271	−1.72821	1.51183	0.03460	0.46746	2.38%	0.69%

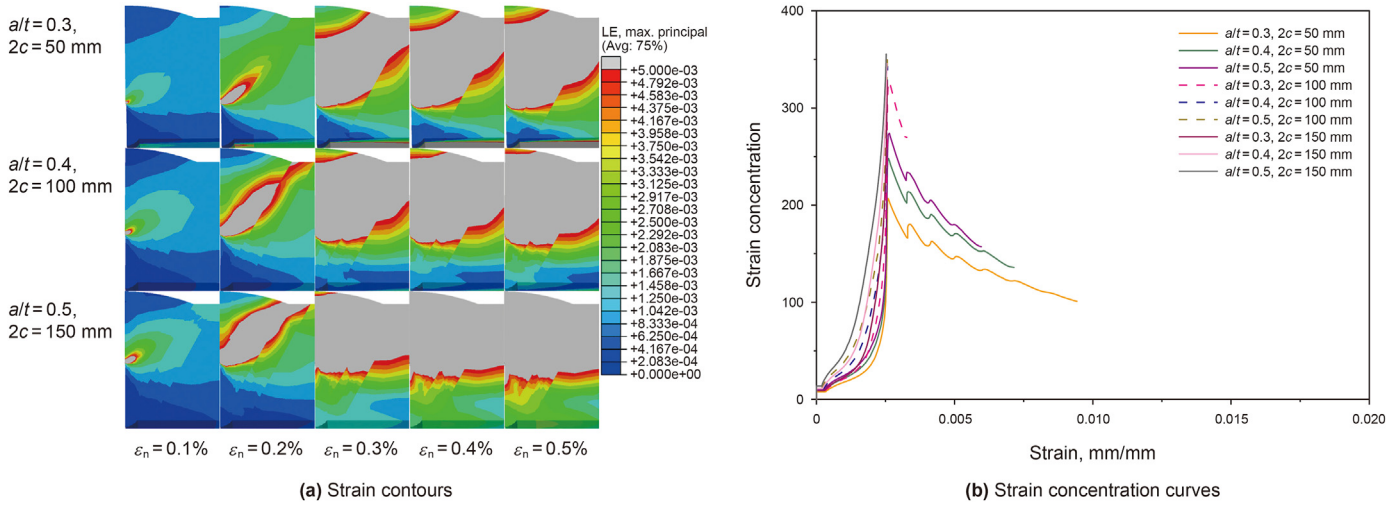

(a) Strain contours **(b)** Strain concentration curves

Fig. 9. Strain contours and strain concentration of girth-welded pipe at different crack sizes: $M = 0.9$, $S = 0.9$.

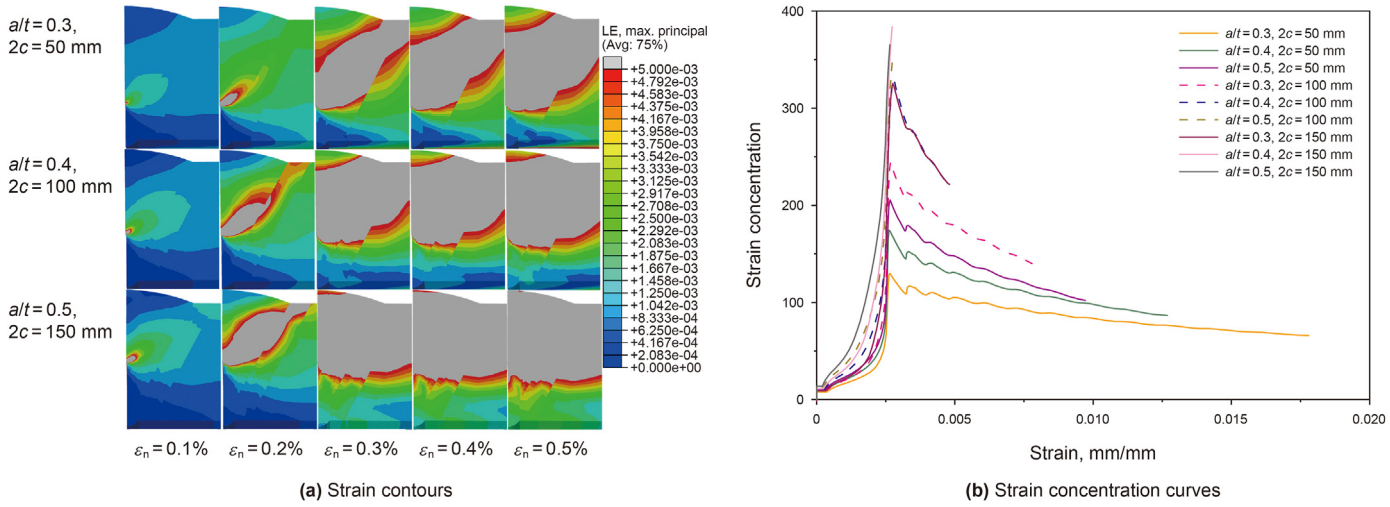

(a) Strain contours **(b)** Strain concentration curves

Fig. 10. Strain contours and strain concentration of girth-welded pipe at different crack sizes: $M = 1.0$, $S = 0.9$.

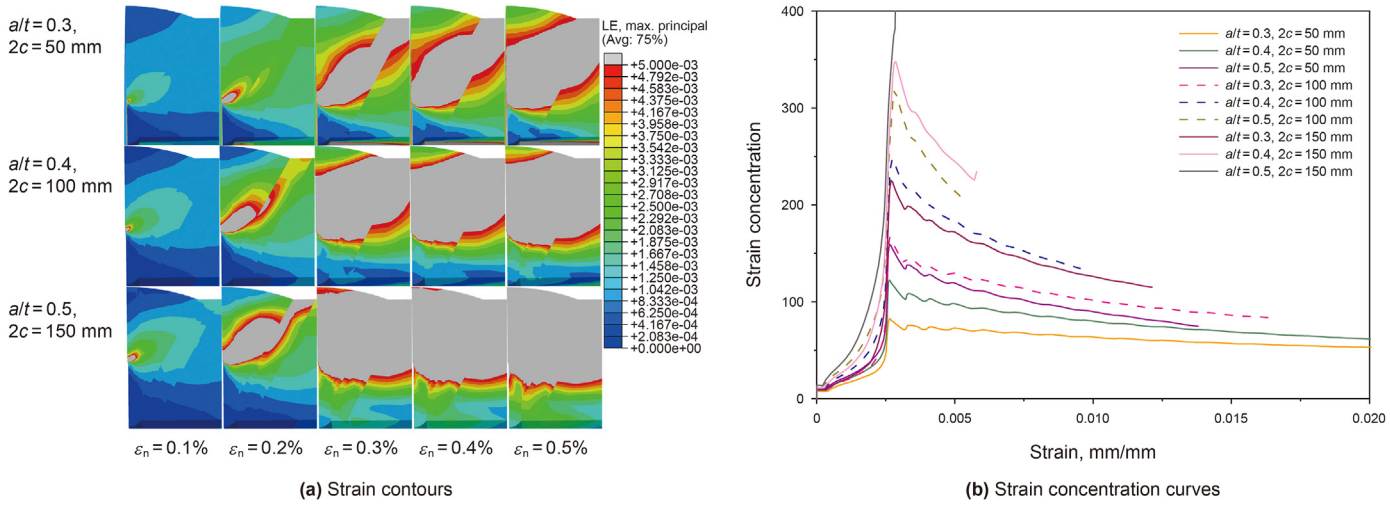

(a) Strain contours **(b)** Strain concentration curves

Fig. 11. Strain contours and strain concentration of girth-welded pipe at different crack sizes: $M = 1.1$, $S = 0.9$.

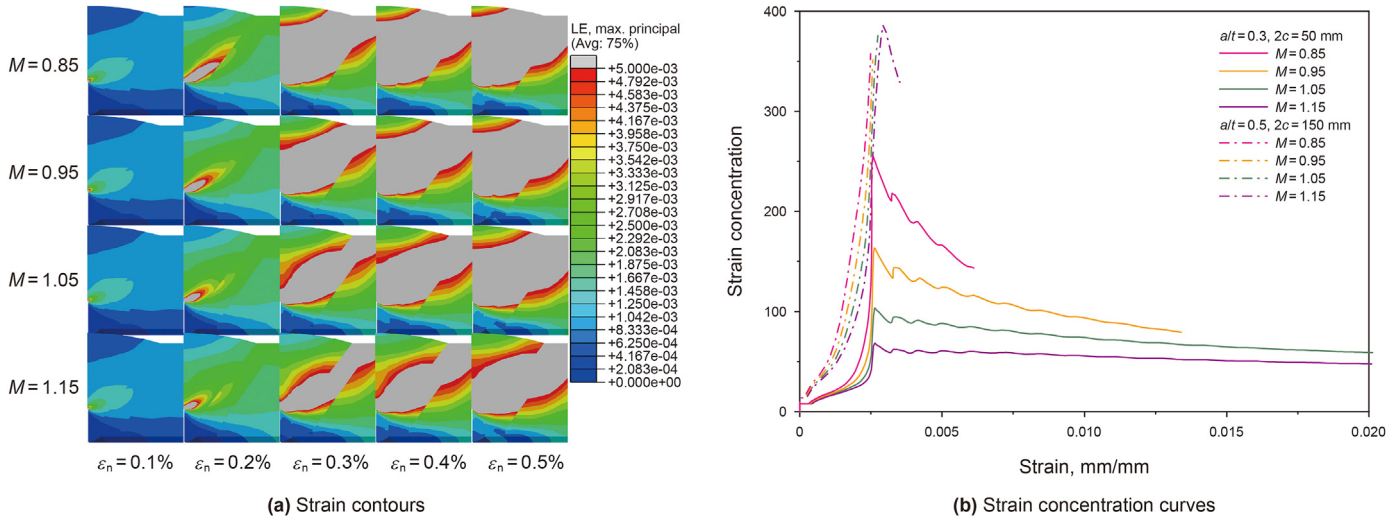

Fig. 12. Strain contours and strain concentration of girth-welded pipe at different mismatch coefficients (M): $S = 0.9$.

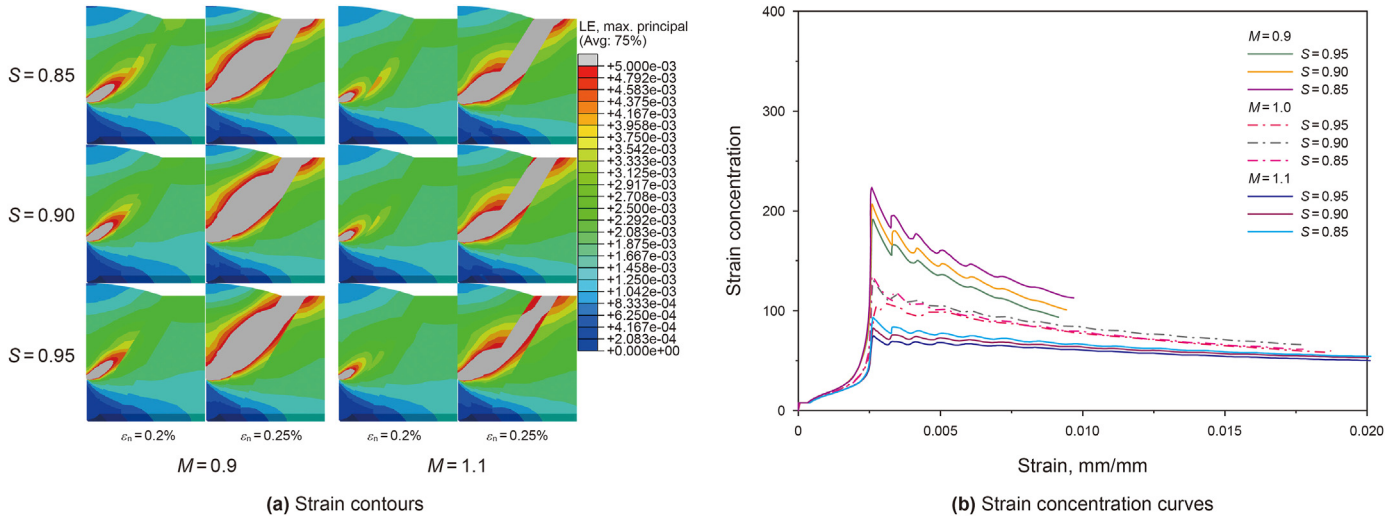

Fig. 13. Strain contours and strain concentration of girth-welded pipe at different softening degrees (S).

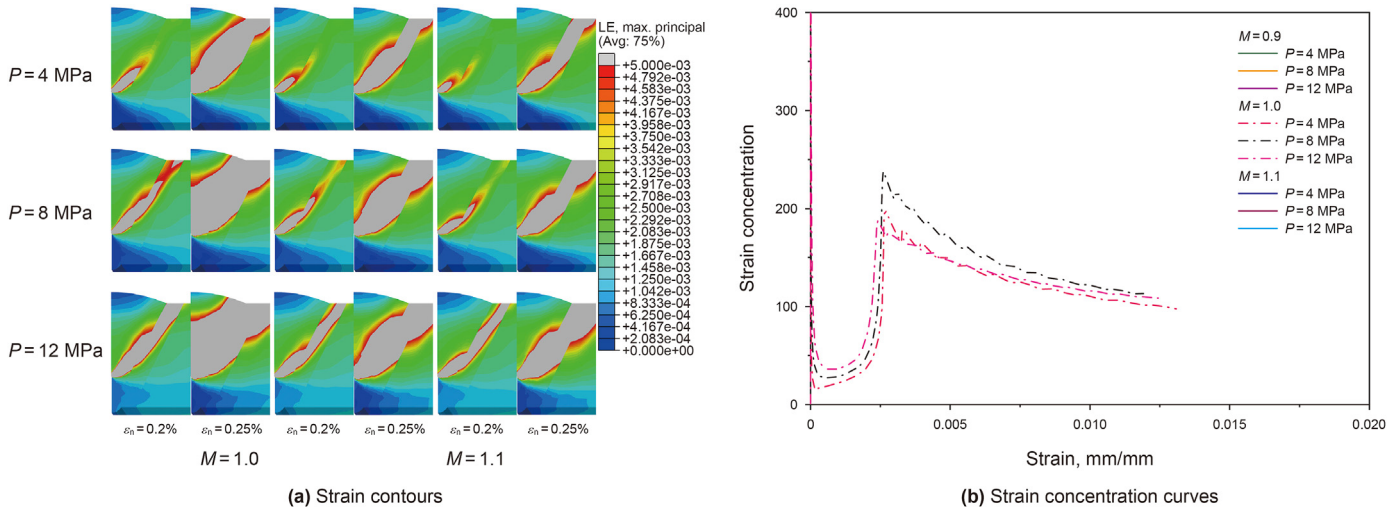

Fig. 14. Strain contours and strain concentration of girth-welded pipe at different internal pressures (P).

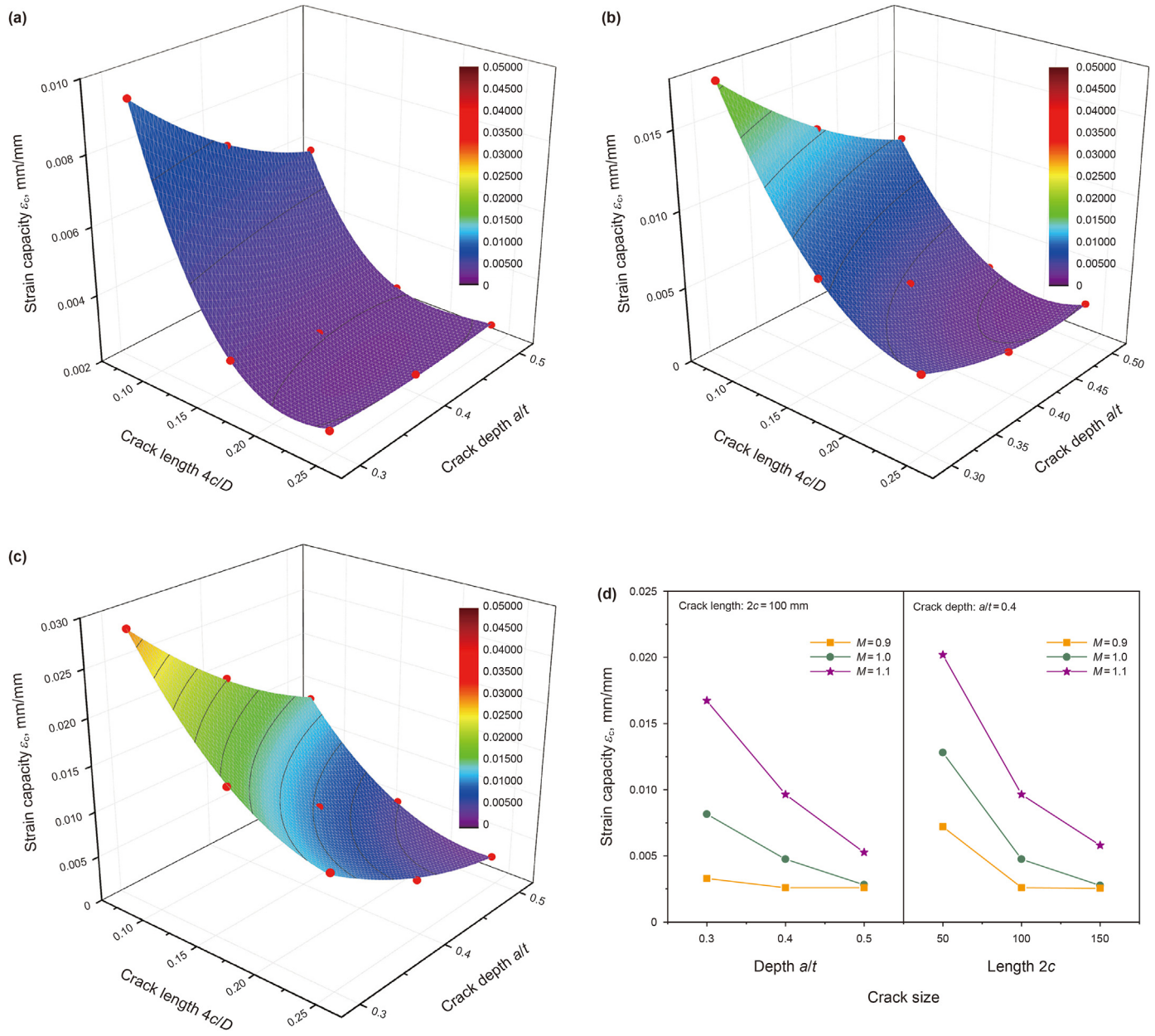

Fig. 15. Effect of crack sizes on strain capacity in mismatch welded: (**a**) $M = 0.9$, (**b**) $M = 1.0$, (**c**) $M = 1.1$, (**d**) different M.

gradually increases. When the internal pressure increases from 8 MPa to 12 MPa, the strain concentration area does not change significantly. Simultaneously, the variation in the strain concentration area is also related to M, and the change in the undermatched weld is more significant than the change of the overmatched weld. In Fig. 14(b), we can see that the influence trend of the internal pressure on the strain concentration factor is independent of M. When the internal pressure is 8 MPa, the value of the strain concentration factor is largest, but the values of 4 MPa and 12 MPa are closer. When the internal pressure increases from 8 MPa to 12 MPa, the strain concentration factor decreases. Due to the Poisson's effect, the internal pressure changes the degree of axial plastic deformation of the girth-welded pipe, which causes the influence of the strain contours and strain concentration factors.

4.2. Effect factors of strain capacity

4.2.1. Defect size

Fig. 15(a, b, c) shows the strain capacity variation of girth-welded pipes under different defect sizes for even-match ($M = 1.0$), undermatch ($M = 0.9$) and overmatch ($M = 1.1$) pipes but with the same degree of softening ($S = 0.9$). The red balls in Fig. 15 represent the original FEA calculation data, and the 3D surfaces are drawn by the formula fitted in Chapter 3. Different colors of rainbows were used to indicate the level of strain capacity in the figures. To clearly compare the strain capacity in different situations, the color scales in all figures adopted unified standards in the following content.

The strain capacity gradually decreases as the depth or length of the crack increases, as shown in Fig. 15. The magnitude of the

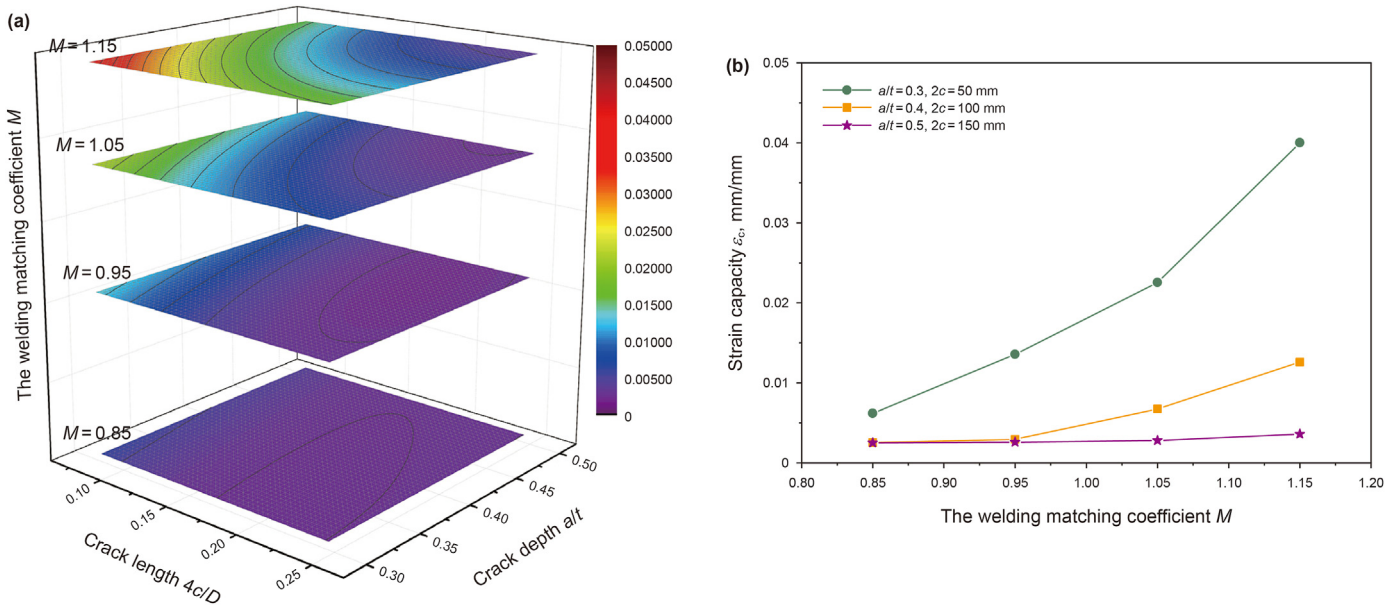

Fig. 16. Effect of weld metal mismatch on strain capacity: (**a**) different *M*, (**b**) different crack size.

change in strain capacity with defect size depends on the welding mismatch coefficient (*M*). As *M* increases, the color gradient in Fig. 15(a, b, c) becomes increasingly distinct, which also means that the strain capacity changes more significantly with a variety of crack sizes. The strain capacity is less sensitive to the crack size in an undermatched weld (smaller *M*, as shown in Fig. 15(a)). At this time, the strain capacity corresponding to the largest defect ($a/t = 0.5, 2c = 150$) is 0.0025, the corresponding strain capacity of the smallest defect ($a/t = 0.3$, $2c = 50$) is 0.0095, and the increase in strain capacity is 280%. The strain capacity is more sensitive to crack size under overmatching (larger *M*, as shown in Fig. 15(c)). In that case, the increment range of the strain capacity between the largest defect and smallest defect is 908%.

Fig. 15(d) further shows the effect of crack size on strain capacity. When the length or depth of the crack is fixed, as the depth or length of the crack increases, the strain capacity of the overmatched welding will change more drastically. At the same time, when the depth or length of the defect is large, the strain capacity is no longer sensitive to the variety of defect sizes.

4.2.2. Mismatch of girth-welded pipe

The variation in strain capacity in girth-welded pipes with different crack sizes but the same degree of softening ($S = 0.9$) under four mismatch coefficients is shown in Fig. 16(a). As *M* increases, the color gradient in Fig. 16(a) becomes more apparent. Fig. 16(b) shows how the strain capacity changes with *M* for three crack sizes. When the defect size is small, the increase in strain capacity with increasing *M* is more evident. The strain capacity increases from 0.0062% to 0.0402%, with an increment of 548%. When the defect size is large, the increment of strain capacity with the increase of *M* is smaller, which is only 44% shown more intuitively in Fig. 12. When the size of the defect is large, the strain concentration area and strain concentration factor are not much different as the remote strain increases. However, when the defect size is small, there is an intuitive gap between the strain concentration area and strain concentration factor.

4.2.3. Softening of HAZ

To study the influence of the softening degree of the HAZ(*S*) on the strain capacity of the girth-welded pipe, various figures of the strain capacity with the crack size under three softening degrees ($S = 0.95, 0.90, 0.85$) were drawn. Fig.s of strain capacity with different softening degrees under even matching ($M = 1.0$), undermatching ($M = 0.9$), and overmatching ($M = 1.1$) were also drawn separately, as shown in Fig. 17(a, b, c). When *M* is larger, as the softening degree increases (the larger the softening degree is, the smaller *S*), the more obvious the color gradient change of the strain capacity. Fig. 17(d) strongly proves that under different crack sizes, the effect of *S* on the strain capacity is very limited under different *M*. The softening of the HAZ has a slight enhancement effect on the strain capacity, which is more obvious when the defect size is small.

4.2.4. Internal pressure

In the case of an even match ($M = 1.0$) and degree of softening ($S = 0.9$), the influence of internal pressure (*P*) on the strain capacity of girth-welded pipes is plotted in Fig. 18(a). As the internal pressure increases, the color gradient becomes inconspicuous, which means that when the internal pressure is greater, the dependence of the strain capacity on the defect size is reduced. Under the design internal pressure ($P = 12$ MPa), the strain capacity and mismatch coefficient (*M*) are also closely related, as shown in Fig. 18(b). As *M* increases, the color gradient becomes significant, which means that in the case of undermatch welding, the effect of crack size on strain capacity is very limited.

As shown in Fig. 18(c and d), these figures further support the above conclusion that internal pressure can reduce strain capacity, and the reduction degree of strain capacity is related to crack size. The smaller the crack size is, the greater the decrease in strain capacity as the internal pressure increases. Taking the crack ($a/t = 0.3$, $2c = 50$ mm) as an example, as the internal pressure increases from 0 to 8 MPa, the strain capacity decreases by 33%, and as the internal pressure further increases to 12 MPa, the strain capacity will be slightly increased by 4.7% due to the influence of the Poisson effect. The strain capacity corresponding to cracks ($a/t = 0.5$, $2c = 150$ mm) decreased only 13% with increasing internal pressure. In the case of different crack sizes, *M* also has an important effect on the reduction in strain capacity caused by internal

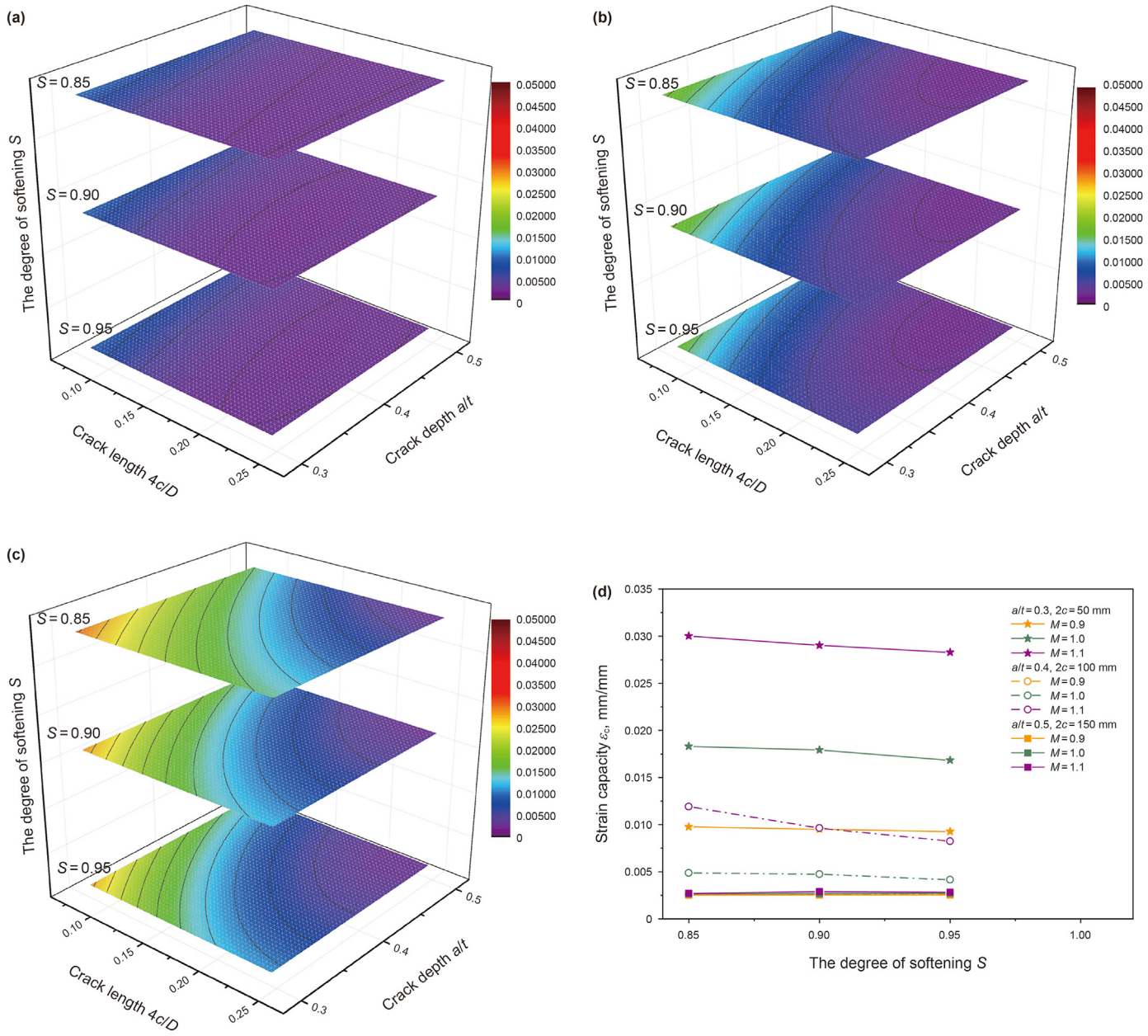

Fig. 17. Effect of HAZ softening on strain capacity: (**a**) $M = 0.9$, (**b**) $M = 1.0$, (**c**) $M = 1.1$,(**d**) different M.

pressure. Taking cracks ($a/t = 0.3$, $2c = 50$ mm) as an example, when M is 0.9, 1.0, and 1.1, the rates of strain capacity reduction caused by internal pressure are 48.2%, 29.8%, and 12.4%, respectively. With increasing M, the reduction rates caused by the internal pressure corresponding to the strain capacity of the crack ($a/t = 0.5$, $2c = 150$ mm) are 14.2%, 13.4%, and 13.2%, respectively.

5. Conclusions

In this paper, girth-welded pipes with cracks in the inner surface of the weld were studied, and crack initiation behavior was simulated using the Gurson model. The corresponding nominal strain at the onset of crack initiation was defined as the characteristic value of the strain capacity. The influencing factors on the strain concentration area, strain concentration factor, and strain capacity of girth-welded pipes have been discussed. A semiempirical calculation formula for the strain capacity for girth-welded X80 grade pipes has been proposed as a function of the crack size (a, 2c), mismatch coefficient (M) of welding, and softening degree (S) of the HAZ. The specific conclusions are as follows.

The strain concentration area in the local area of a girth-weld pipe will be affected by defects, mismatch coefficient, softening degree, and internal pressure. When the remote strain is less than 0.3%, the influence trend is more obvious. When the remote strain increases from 0.3% to 0.5%, the differences caused by various influencing factors gradually diminish.

The strain concentration factor at the crack tip reaches its maximum value when the remote strain is approximately 0.25%. When the size of the defect is large and the mismatch coefficient M is small, the crack will start to grow at the maximum value of the strain concentration factor. Otherwise, the crack will grow at a smaller strain concentration factor.

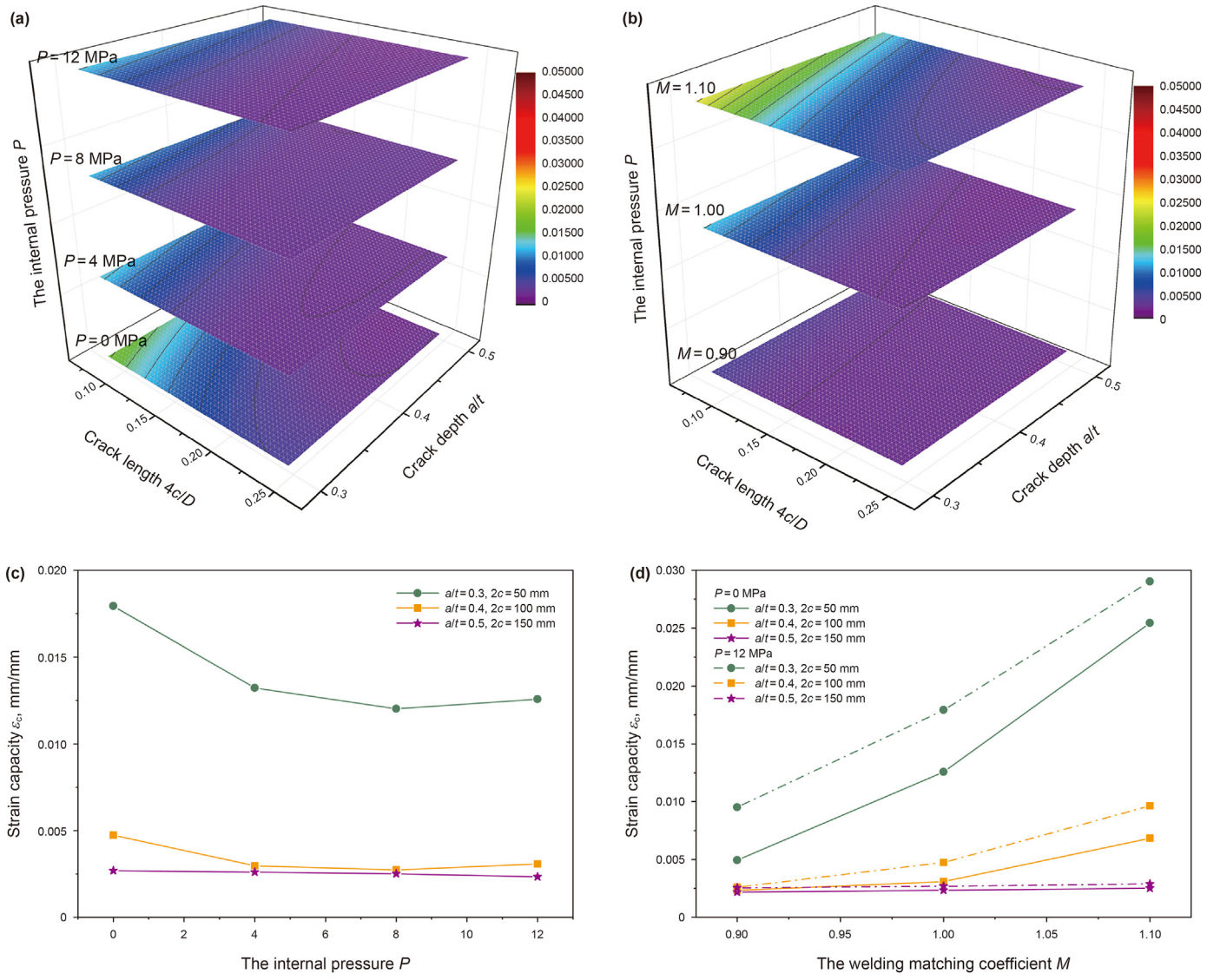

Fig. 18. Effect of HAZ softening on strain capacity: (**a**) (**c**) different *P*, (**b**) (**d**) different *M*.

The dependence of the strain capacity on defects is related to M. The strain capacity in the overmatch of the girth-welded pipe is more sensitive to the crack size. When the crack is large and M is small, the sensitivity of the strain capacity to influencing factors will decrease. When the defect is located in the weld, the softening of the HAZ has a slight enhancement effect on the strain capacity but is very limited.

The internal pressure can reduce the strain capacity, and the reduction in the strain capacity is related to the crack size. The smaller the crack size is, the greater the decrease in strain capacity as the internal pressure increases. When the internal pressure is 8 MPa, the value of the strain capacity is the smallest. However, when the internal pressure increases to 12 MPa, the strain capacity increases slightly. In the case of different crack sizes, *M* also has an important effect on the reduction in strain capacity caused by internal pressure.

Acknowledgements

This research is supported by the grants from the National Natural Science Foundation of China (Grant No. 51874324). The author also want to thank the Chinese Scholarship Council (CSC) for the financial support.

References

Abdulhameed, D., Cakiroglu, C., Lin, M., et al., 2016. The effect of internal pressure on the tensile strain capacity of X52 pipelines with circumferential flaws. J. Pressure Vessel Technol. Trans. ASME 138 (6). https://doi.org/10.1115/1.4033436.

Agbo, S., Lin, M., Ameli, I., et al., 2019. Experimental evaluation of the effect of the internal pressure and flaw size on the tensile strain capacity of welded X42 vintage pipelines. Int. J. Pres. Ves. Pip. 173, 55–67. https://doi.org/10.1016/j.ijpvp.2019.04.010.

AS, D.N.V., 2017. In: Submarine Pipeline Systems. Technical report, DNV-OS-F101.

Bastola, A., Wang, J., Shitamoto, H., et al., 2016. Full- and small-scale tests on strain capacity of X80 seamless pipes. In: 21st European Conference on Fracture, vol. 2, pp. 1894–1903. https://doi.org/10.1016/j.prostr.2016.06.238. Ecf21.

Bastola, A., Wang, J., Shitamoto, H., et al., 2017. Investigation on the strain capacity of girth welds of X80 seamless pipes with defects. Eng. Fract. Mech. 180, 348–365. https://doi.org/10.1016/j.engfracmech.2017.06.010.

Cravero, S., Bravo, R.E., Ernst, H.A., 2008. Constraint evaluation and effects on JR resistance curves for pipes under combined load conditions. In: The Eighteenth International Offshore and Polar Engineering Conference. International Society of Offshore and Polar Engineers.

Di, Y., Shuai, J., Wang, J.Q., et al., 2015. A new specimen for high-grade pipeline steels CTOA test. Eng. Fract. Mech. 148, 203–212. https://doi.org/10.1016/

j.engfracmech.2015.06.088.
Gurson, A.L., 1977. Continuum theory of ductile rupture by void nucleation and growth .I. Yield criteria and flow rules for porous ductile media. J. Eng. Mater. Technol. Trans. ASME 99 (1), 2–15. https://doi.org/10.1115/1.3443401.
Han, K.J., Shuai, J., Deng, X.M., et al., 2014. The effect of constraint on CTOD fracture toughness of API X65 steel. Eng. Fract. Mech. 124–125, 167–181. https://doi.org/10.1016/j.engfracmech.2014.04.014.
Hertelé, S., De Waele, W., Denys, R., et al., 2013. Weld strength mismatch in strain based flaw assessment: which definition to use? J. Pressure Vessel Technol. 135 (6). https://doi.org/10.1115/1.4025343.
Hertelé, S., O'Dowd, N., Van Minnebruggen, K., et al., 2014. Effects of pipe steel heterogeneity on the tensile strain capacity of a flawed pipeline girth weld. Eng. Fract. Mech. 115, 172–189. https://doi.org/10.1016/j.engfracmech.2013.11.003.
Hertele, S., Van Minnebruggen, K., Verstraete, M., et al., 2016. Influence of pipe steel heterogeneity of the upper bound tensile strain capacity of pipeline girth welds: a validation study. Eng. Fract. Mech. 162, 121–135. https://doi.org/10.1016/j.engfracmech.2016.03.042.
Hohler, S., Karbasian, H., Gering, A., et al., 2016–2017. Strain capacity of large diameter pipes: full scale investigation with influence of girth weld, strip end weld and ageing effects. In: Proceedings of the 11th International Pipeline Conference, vol. 2. https://doi.org/10.1115/IPC2016-64151.
Igi, S., Sakimoto, T., Endo, S., 2011. Effect of internal pressure on tensile strain capacity of X80 pipeline. In: 11th International Conference on the Mechanical Behavior of Materials, vol. 10, pp. 1451–1456. https://doi.org/10.1016/j.proeng.2011.04.241. Icm11.
Kibey, S., Issa, J., Minnaar, K., et al., 2008. Effect of misalignment on the tensile strain capacity of welded pipelines. In: The Eighteenth International Offshore and Polar Engineering Conference. International Society of Offshore and Polar Engineers.
Kyriakides, S., Corona, E., 2007. Mechanics of Offshore Pipelines: Volume 1 Buckling and Collapse, vol. 1. Elsevier.
Liu, M., Wang, Y.Y., 2006. Applying Gurson type of damage models to low constraint tests of high strength steels and welds. In: 2006 International Pipeline Conference. American Society of Mechanical Engineers Digital Collection. https://doi.org/10.1115/IPC2006-10416.
Maddox, S.J., 2014. Fatigue Strength of Welded Structures. Woodhead publishing.
Ostby, E., Hellesvik, A.O., 2008. Large-scale experimental investigation of the effect of biaxial loading on the deformation capacity of pipes with defects. Int. J. Pres. Ves. Pip. 85 (11), 814–824. https://doi.org/10.1016/j.ijpvp.2008.04.009.
Østby, E., Nyhus, B., Hauge, M., et al., 2008. Strain capacity of SENT specimens-Influence of weld metal mismatch and ductile tearing resistance. In: The Eighteenth International Offshore and Polar Engineering Conference. International Society of Offshore and Polar Engineers.
Panico, M., Tang, H., Fairchild, D., et al., 2017. ExxonMobil SENT test method and application to Strain-Based Design. Int. J. Pres. Ves. Pip. 156, 17–22. https://doi.org/10.1016/j.ijpvp.2017.06.010.
Pineau, A., 2006. Development of the local approach to fracture over the past 25 years: theory and applications. Int. J. Fract. 138 (1–4), 139–166.
Qiang, B., Wang, X., 2019. Ductile crack growth behaviors at different locations of a weld joint for an X80 pipeline steel: a numerical investigation using GTN models. Eng. Fract. Mech. 213, 264–279. https://doi.org/10.1016/j.engfracmech.2019.04.009.
Revie, R.W., 2015. Oil and Gas Pipelines: Integrity and Safety Handbook. John Wiley & Sons.
Sandvik, A., Ostby, E., Thaulow, C., 2008. A probabilistic fracture mechanics model including 3D ductile tearing of bi-axially loaded pipes with surface cracks. Eng. Fract. Mech. 75 (1), 76–96. https://doi.org/10.1016/j.engfracmech.2007.02.015.
Testa, G., Bonora, N., Gentile, D., et al., 2017. Strain capacity assessment of API X65 steel using damage mechanics. Frat. Ed. Integrità Strutt. (42), 315–327. https://doi.org/10.3221/IGF-ESIS.42.33.
Tu, S.W., Ren, X.B., He, J.Y., et al., 2019. Experimental measurement of temperature-dependent equivalent stress-strain curves of a 420 MPa structural steel with axisymmetric notched tensile specimens. Eng. Fail. Anal. 100, 312–321. https://doi.org/10.1016/j.engfailanal.,2019.02.043.
Tu, S.W., Ren, X.B., Nyhus, B., et al., 2017. A special notched tensile specimen to determine the flow stress-strain curve of hardening materials without applying the Bridgman correction. Eng. Fract. Mech. 179, 225–239. https://doi.org/10.1016/j.engfracmech.2017.04.039.
Tvergaard, V., 1982. On localization in ductile materials containing spherical voids. Int. J. Fract. 18 (4), 237–252.
Tvergaard, V., Needleman, A., 1984. Analysis of the cup-cone fracture in a round tensile bar. Acta Metall. 32 (1), 157–169. https://doi.org/10.1016/0001-6160(84)90213-X.
Van Minnebruggen, K., Hertele, S., Thibaux, P., et al., 2015. Effects of specimen geometry and anisotropic material response on the tensile strain capacity of flawed spiral welded pipes. Eng. Fract. Mech. 148, 350–362. https://doi.org/10.1016/j.engfracmech.2015.04.031.
Verstraete, M., De Waele, W., Denys, R., et al., 2014. Constraint analysis of defects in strength mismatched girth welds of (pressurized) pipe and Curved Wide Plate tensile test specimens. Eng. Fract. Mech. 131, 128–141. https://doi.org/10.1016/j.engfracmech.2014.07.018.
Wang, X., Kibey, S., Tang, H., et al., 2011. Strain-based design-advances in prediction methods of tensile strain capacity. Int. J. Offshore Polar Eng. 21 (1), 1–7.
Wang, X., Shuai, J., Lv, Z.Y., 2020. Study on FAD curves of steel pipes based on stress-strain curves. In: Theoretical and Applied Fracture Mechanics, vol. 106. https://doi.org/10.1016/j.tafmec.2019.102451.
Xu, J., Zhang, Z.L., Østby, E., et al., 2009. Effects of crack depth and specimen size on ductile crack growth of SENT and SENB specimens for fracture mechanics evaluation of pipeline steels. Int. J. Pres. Ves. Pip. 86 (12), 787–797. https://doi.org/10.1016/j.ijpvp.2009.12.004.
Zhang, Z.L., Ødegård, J., Thaulow, C., 1998. Characterization of material ductility by microvoid nucleation parameters. In: Proceeding of the 19th Risù International Symposium on Material Science: Modelling of Structure and Mechnaics of Materials from Microscale to Product. Risù, Denmark.
Zhang, Z.L., Thaulow, C., Ødegård, J., 2000. A complete Gurson model approach for ductile fracture. Eng. Fract. Mech. 67 (2), 155–168. https://doi.org/10.1016/S0013-7944(00)00055-2.
Zhao, X.X., Xu, L.Y., Jing, H.Y., et al., 2019. A strain-based fracture assessment for offshore clad pipes with ultra undermatched V groove weld joints and circumferential surface cracks under large-scale plastic strain. Eur. J. Mech. Solid. 74, 403–416. https://doi.org/10.1016/j.euromechsol.2018.12.002.
Zhu, X.K., 2015. State-of-the-art review of fracture control technology for modern and vintage gas transmission pipelines. Eng. Fract. Mech. 148, 260–280. https://doi.org/10.1016/j.engfracmech.2015.05.055.